International Journal of
Molecular Sciences

MDPI

Article

Experimental and Computational Studies on the Interaction of a Dansyl-Based Fluorescent Schiff Base Ligand with Cu^{2+} Ions and CuO NPs

Jesús Sanmartín-Matalobos [1], Pilar Bermejo-Barrera [2], Ignacio Pérez-Juste [3], Matilde Fondo [1], Ana M. García-Deibe [1,*] and Yeneva Alves-Iglesias [1,2]

[1] Coordination and Supramolecular Chemistry Group (SupraMetal), Institute of Materials (iMATUS), Department of Inorganic Chemistry, Faculty of Chemistry, Universidade de Santiago de Compostela, Avenida das Ciencias s/n, 15782 Santiago de Compostela, Spain
[2] Trace Element, Speciation and Spectroscopy Group (GETEE), Institute of Materials (iMATUS), Department of Analytical Chemistry, Nutrition and Bromatology, Faculty of Chemistry, Universidade de Santiago de Compostela, Avenida das Ciencias s/n, 15782 Santiago de Compostela, Spain
[3] Departamento de Química Física, Facultad de Química, Edificio de Ciencias Experimentales, Universidade de Vigo, 36310 Vigo, Spain
[*] Correspondence: ana.garcia.deibe@usc.es

Abstract: We studied the interaction of Cu^{2+} ions and CuO nanoparticles with the fluorescent Schiff base ligand H_3L, which derives from the condensation of 4-formyl-3-hydroxybenzoic acid with *N*-(2-aminobenzyl)-5-(dimethylamino)naphthalene-1-sulfonamide (DsA). A detailed assignment of the most significant bands of the electronic and infrared spectra of H_3L and DsA was performed using DFT methods, based on both crystal structures. The affinity of H_3L to react with Cu^{2+} ions in solution ($K_B = 9.01\ 10^3$ L mol^{-1}) is similar to that found for the Cu^{2+} ions present on the surface of CuO NPs ($K_B = 9.84\ 10^3$ L mol^{-1}). Fluorescence spectroscopic measurements suggest five binding sites for H_3L on the surface of the CuO NPs used. The μ-XRF analysis indicates that a polycrystalline sample of CuO-H_3L NPs contains 15:1 Cu:S molar ratio (CuO:H_3L). ATR-FTIR spectroscopy, supported by DFT calculations, showed that the HL^{2-} (as a phenolate and sulfonamide anion) is coordinated to superficial Cu^{2+} ions of the CuO NPs through their azomethine, sulphonamide, and phenolic groups. A solution of H_3L (126 ppb) shows sensitive responses to CuO NPs, with a limit of detection (LOD) of 330 ppb. The working range for detection of CuO NPs with $[H_3L]$ = 126 ppb was 1.1–9.5 ppm. Common metal ions in water, such as Na^+, K^+, Mg^{2+}, Ca^{2+}, Fe^{3+}, and Al^{3+} species, do not interfere significantly with the detection of CuO NPs.

Keywords: CuO nanoparticles; nanomaterials; detection; luminescence; Schiff base; fluorescent chemosensor; fluorescence quenching

check for updates

Citation: Sanmartín-Matalobos, J.; Bermejo-Barrera, P.; Pérez-Juste, I.; Fondo, M.; García-Deibe, A.M.; Alves-Iglesias, Y. Experimental and Computational Studies on the Interaction of a Dansyl-Based Fluorescent Schiff Base Ligand with Cu^{2+} Ions and CuO NPs. *Int. J. Mol. Sci.* **2022**, *23*, 11565. https://doi.org/10.3390/ijms231911565

Academic Editor: Barbara Miroslaw

Received: 27 August 2022
Accepted: 23 September 2022
Published: 30 September 2022

1. Introduction

The unique properties of metal and metal oxide nanomaterials have led to their widespread use in daily life [1–5], which has the clear negative effect of an increasing release of these nanomaterials into the environment [6–10]. Particularly, CuO NPs are manufactured on a large scale for their varied industrial and domestic applications, as they are generally considered to be non-toxic. Thus, one of the common usages of CuO NPs is in water treatment, as an effective adsorbent of several pollutants [4]. However, some concern is arising about the possible adverse health and environmental effects of their release since several studies claim that CuO NPs could have negative impacts on different living organisms [11–13].

Therefore, the development and improvement of methods for the detection of CuO NPs is a growing field of study. Thus, Zhao et al. used EDS analysis to quantify the presence of copper on the root surface of an aquatic plant, after CuO NP exposure [14]. ICP-OES was used by Peng et al. to measure the copper content in root of rice after adding CuO NPs to the soil [15], while Navratilova et al. applied the single particle ICP-MS method for the detection of CuO NPs in colloidal extracts from natural soil samples [16]. In this sense, our research group has also used a pyrrole-based [17], as well as phenol-based Schiff base ligands [18] as fluorescent sensors for the detection of CuO NPs (LOD = 13.83 and 9.80 μgL^{-1}, respectively). These two *N*-tosyl imines have a moderate fluorescence emission, which drastically decreases by interaction with copper ions present on the surface of the CuO NPs. In the present study, with the aim of avoiding the disadvantages of using weakly fluorescent ligands, we designed a new sensor with higher fluorescence emission intensity providing potential N and O donor atoms, which have demonstrated to be suitable for coordinating those superficial copper ions present on the surface of the CuO nanoparticles [17,18].

We investigated the ability of the dansyl-based fluorescent Schiff base ligand H_3L for detecting CuO NPs in ethanol-water solutions, with short response time and sensing at basic pH. H_3L can be easily synthesized (Scheme 1) from the condensation of 4-formyl-3-hydroxybenzoic acid with *N*-(2-aminobenzyl)-5-(dimethylamino)naphthalene-1-sulfonamide (DsA). This dansyl-derived amine had been previously obtained by selective reaction of 2-(aminomethyl)aniline with dansyl chloride [19]. H_3L displays an *N,N,O*-binding domain suitable to interact with Cu^{2+} ions, either in solution, or as constituents of a solid matrix as CuO NPs. In this case, additional O atoms belonging to carboxylate and sulfonamide groups can also be involved in the interaction.

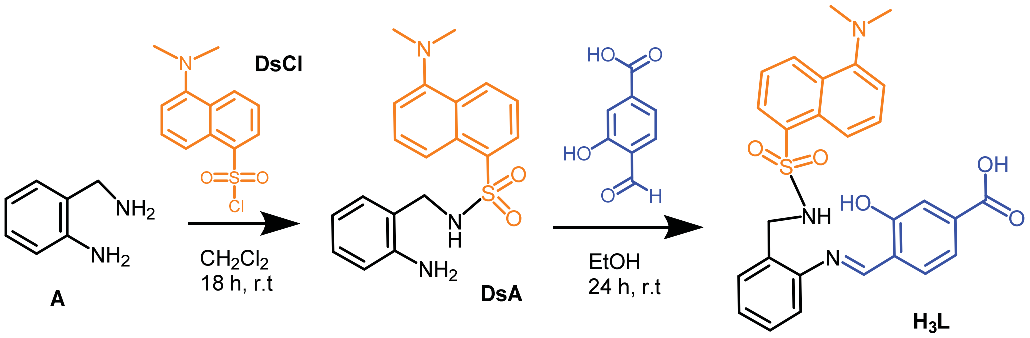

Scheme 1. Schematic representation of the synthesis of H_3L in two steps: (i) selective dansylation of a primary diamine and (ii) aldiminic condensation of DsA with 4-formyl-3-hydroxybenzoic acid.

Since the knowledge of the surface coordination chemistry of NPs [20–23] is advantageous for the development of chemical sensors for them, we also present here some experimental and computational studies on the interactions of H_3L with CuO NPs. SEM-EDX, μ-XRF, ATR-IR, and DFT were used to investigate the interaction of H_3L with the surface of CuO NPs. With the aim of assisting in the interpretation of the results obtained from the study of the interaction between H_3L and CuO NPs, the copper(II) complex, $Cu_2L_2(H_2O)_4$, was synthesized and studied by ATR-IR, UV-Vis, and fluorescence spectroscopies. DFT calculations have been used to predict the effect of the symmetry of DsA, H_3L, and $Cu_2L_2(H_2O)_4$ on their vibrational modes and electronic properties. Binding constants have been also determined since these constants characterize the affinity of H_3L for both NMs and ions. Changes in the fluorescence emission spectra of H_3L upon increasing addition of CuO NPs have been investigated as well, while taking into consideration possible interferences from some common metal ions in water.

2. Results and Discussion

With the aim of investigating the ability of a dansyl-based fluorescent Schiff base ligand for detecting copper oxide nanomaterials in ethanol-water samples, we designed the easily synthesized H_3L (Scheme 1). An ethanol solution of H_3L at neutral pH emitted a maximal green fluorescence at about 524 nm, when it was exposed to radiation with a wavelength of 400 nm. This fluorescent behavior was assigned to the dansyl moiety, which is well known for a typical charge-transfer band between the donor dimethylamino group and the sulfonyl group [24].

H_3L can be obtained in a quick two-step synthesis (Scheme 1). In the first step, 2-(aminomethyl)aniline selectively reacts, through the aminomethyl group, with dansyl chloride to yield *N*-(2-aminobenzyl)-5-(dimethylamino)naphthalene-1-sulfonamide (DsA). Subsequent nucleophilic addition of DsA to 4-formyl-3-hydroxybenzoic acid leads to the desired Schiff base ligand H_3L [19]. Both reactions were performed at room temperature, in order to prevent the dansylation of both amino groups in the first step, as well as undesired chemical reactions of DsA in the second step. Spectroscopic characterization details of H_3L and DsA, obtained as powdery solids, are shown in the experimental section. Figures S1 and S2 show the ^{1}H NMR spectra of H_3L and DsA (in dmso-d$_6$), respectively. Single crystals of $[H_4L]Cl\cdot 0.92H_2O$ were obtained by slow evaporation of an ethanol solution of DsA and 4-formyl-3-hydroxybenzoic acid, to which triethylammonium chloride ($[HNEt_3]^+$, $pK_a = 10.75$) had been added.

2.1. Crystal Structures for H_3L and DsA

The molecular structure of two neighboring $[H_4L]^+$ cations is shown in Figure 1, as an ellipsoid diagram, which includes a labelling scheme equivalent to that used in the crystal structure of DsA (see below). Some significant crystal parameters and refinement data are summarized in Table S1. The asymmetric unit of $[H_4L]Cl\cdot 0.92H_2O$ consists of two crystallographically independent cationic moieties of $[H_4L]^+$, showing their amine N atoms protonated (N33 and N73), two chloride counterions, and several water molecules with low occupation sites, which sum up to 0.92, per asymmetric unit. It must be noted that one of the chloride anions, as well as one of the dansyl residues (C63–C75) are disordered on two different occupation sites (0.832 and 0.168).

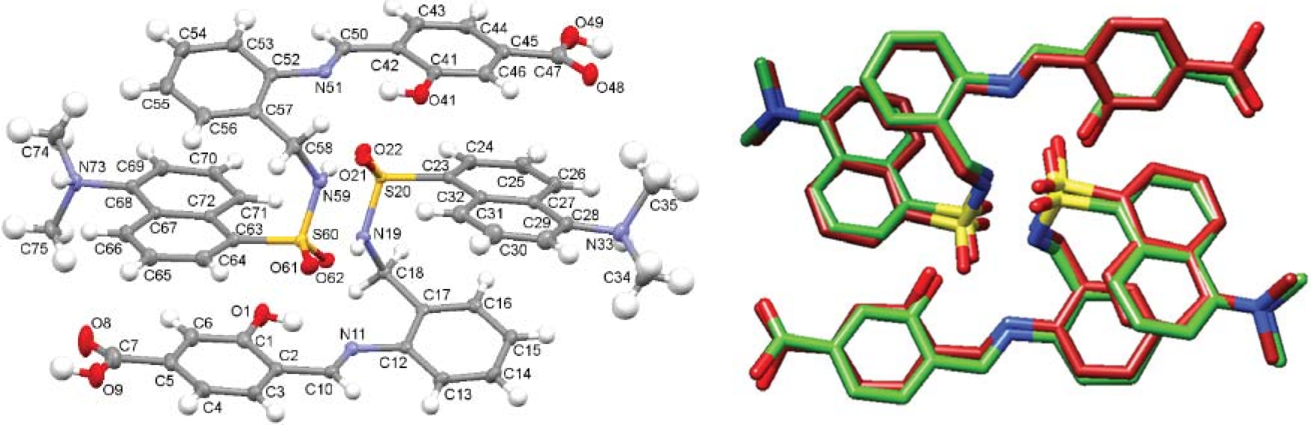

Figure 1. (**Left**): Ellipsoid view of the molecular structure of the two H_4L^+ cations present in the asymmetric unit of $[H_4L]Cl\cdot 0.92H_2O$ crystals. (**Right**): Superimposition of the experimental structure and the theoretically calculated one (M062X/6-31G*) as sticks diagrams.

Geometric parameters (Tables S2 and S3) are within typical ranges observed for residues related to DsA [25–28] and 4-formyl-3-hydroxybenzoic acid [29–31]. Strong intramolecular H bonds (Table S4) O(1)-H(1)···N(11) and O(41)-H(41)···N(51), as well as π-stacking interactions stabilize the configuration of these two molecules. Mutual intermolecular bonds, N(19)-H(19)···O(61), and N(59)-H(59)···O(21), are responsible for connecting adjacent molecules, which as a result are forming H-bonded dimers shown in Figure 1. The crystal packing is reinforced through interactions between HMe_2N^+- and HOOC- groups with solvated water molecules, as well as with chloride counterions.

Since the experimental geometry available for the H_3L ligand corresponds to that of two neighboring cationic units found in the $[H_4L]Cl\cdot 0.92\ H_2O$ crystal, these data were used to obtain the theoretical structure for a H-bonded dimer of H_3L (Figure S3). This

M062X/6-31G* optimized geometry shows an excellent agreement with the structure of the asymmetric unit of the $[H_4L]Cl \cdot 0.92H_2O$ crystal (Figure 1, right), with differences between experimental and theoretical values for bond lengths and bond angles lower than 0.06 Å and 3.5°, respectively (Table S5).

Moreover, we solved the crystal structure of the precursor DsA, which is shown in Figure 2. Details of the crystal data collection and structure refinement are also summarized in Table S1. Crystals of DsA consist of crystallographically independent molecules, whose main geometric parameters (Tables S2 and S3) are within the typical ranges observed for other dansyl derivatives [25–28]. Mutual intermolecular N(19)-H(19A)$\cdots$O(21)$^{\#3}$ bonds allow connecting two contiguous molecules to form H-bonded dimers, as occurred for its derivative $[H_4L]Cl \cdot 0.92\ H_2O$ as well. Sulfonamide oxygen atoms of DsA are additionally connected to other adjacent molecules through the amino group N(11)-H(11B)$\cdots$O(21)$^{\#4}$ (Table S6), as typically observed for dansyl [25] and tosyl [32] derivatives.

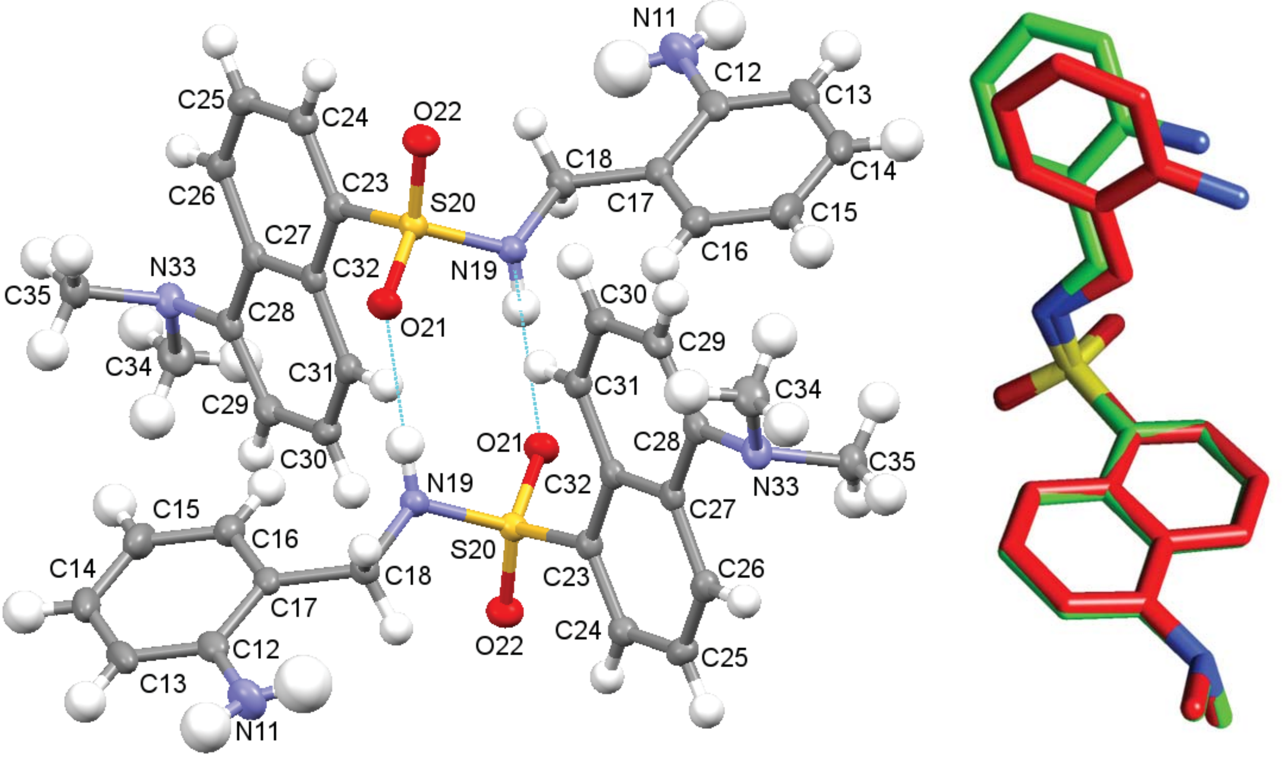

Figure 2. (**Left**): Ellipsoid diagram of the molecular structure found for DsA, including its labelling scheme. Two neighboring molecules are showing their mutual interaction. (**Right**): Superimposition of the stick diagrams of the experimental structure and the calculated one (M062X/6-31G*) for a single unit of DsA.

Taking this crystallographic information as a starting point, we also obtained the M062X/6-31G* optimized geometry for a single unit of DsA (Figure S4). The good agreement between the experimental structure and the calculated one is shown in Figure 2 (right), with differences for bond lengths and bond angles lower than 0.05 Å and 3.5°, respectively (Table S7). The theoretical conformational analysis of DsA supports that the preference for the experimentally crystal structure here presented is related to the stabilization facilitated by hydrogen bonds between adjacent molecules in the solid phase.

2.2. Electronic and Vibrational Spectra of H_3L and DsA

DFT calculations at the M062X/6-31G* level of theory were used to assist in the correct assignment of bands in the electronic and vibrational spectra of H_3L and DsA.

The theoretical electronic spectrum of DsA (Figure 3) shows three dominant signals around 180, 220, and 295 nm that appear about 50–70 nm blue-shifted, with respect to the bands experimentally observed (252, 294, and 346 nm). The analysis of their natural transition orbitals (Table 1) indicates that the band at higher wavelengths mainly corresponds to a π-π* transition in the dansyl residue. The band at 220 nm corresponds to a markedly mixed n-π* and π-π* transition in the dansyl unit as well. Finally, among the several electronic transitions that contribute to the intense band at lower wavelengths, the most intense ones are two π-π* transitions located in the dansyl unit, and a π-π* transition located in the aniline moiety.

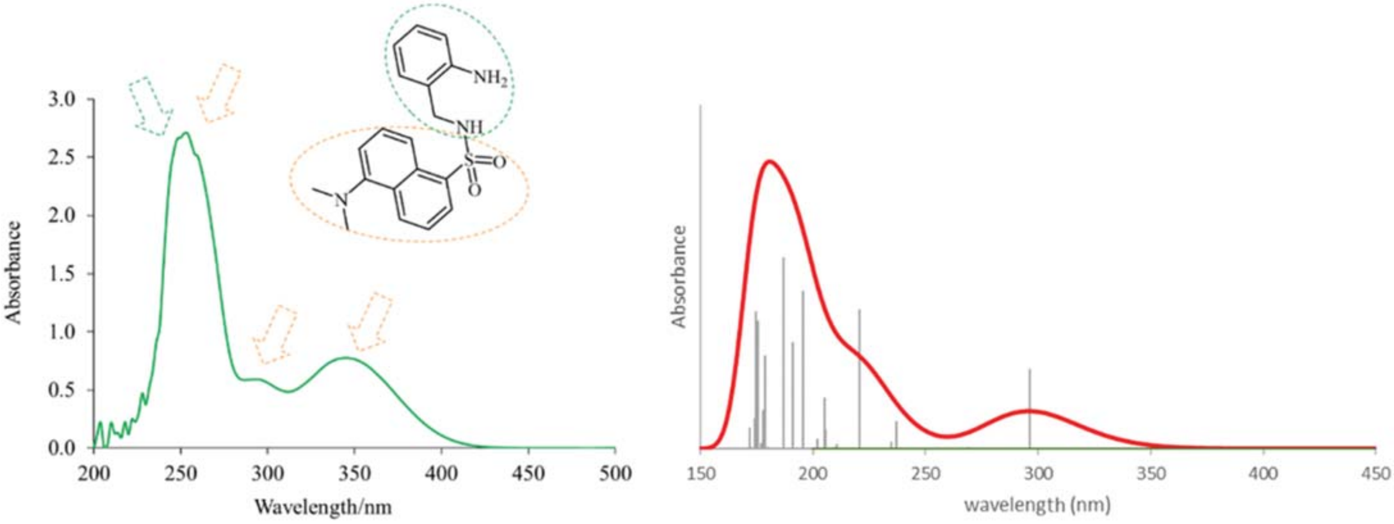

Figure 3. Experimental (**left**) and theoretical (**right**) profiles for the electronic spectrum of DsA. The signal assignment of the two moieties of the molecule has been included as a schematic. The orange arrows show the bands associated with the dansyl moiety, and the green arrow shows the band associated with the aniline moiety. Vertical lines indicate individual electronic transitions listed in Table 1.

The theoretical electronic spectrum of H_3L (Figure 4, right) also shows three dominant signals located around 323, 263, and 224 nm, which appear blue-shifted with respect to those experimentally observed (340, 248, and 224 nm) (Figure 4, left). The analysis of the molecular orbitals involved in each electronic transition of H_3L, and the corresponding natural transition orbitals (Table 2), indicates that the bands at 323 and 263 nm correspond to π-π* transitions mainly centered in the quasi-planar and conjugated hydroxybenzoic/aniline region. The occupied orbital for the transition at 263 nm also shows a noticeable contribution from orbitals centered in the C=N group. The low wavelength maximum at 224 nm corresponds to a strongly mixed transition, which can also be mainly characterized as a π-π* transition centered in the orbitals of the π- stacked aromatic rings.

The assignment of the more significant bands of the infrared spectra of H_3L (Table 3) and DsA (Table 4) has also been done on the basis of the calculated spectrum using DFT methods. The IR spectrum of H_3L shows a characteristic new strong sharp band at about 1613 cm^{-1}, which is attributable to the formation of the imino group (Table 3). This band evidences the condensation through the amino group of DsA with the 4-formyl-3-hydroxybenzoic acid. Furthermore, as a result of this condensation, the absence of the two bands at about 3470 and 3383 cm^{-1}, attributable to ν_a NH_2 and ν_s NH_2 modes, respectively, is clear in the spectrum of DsA. Figures S5 and S6 show the experimental and calculated IR spectra of H_3L and DsA, respectively. The characteristic $O\text{-}H_{(phenol)}$ and $N\text{-}H_{(sulfonamide)}$ stretches are observed as a single signal at 3283 cm^{-1} in the spectrum of H_3L. Asymmetric and symmetric O=S=O stretches can also be clearly observed at about 1315 and 1140 cm^{-1}, respectively, in the IR spectra of H_3L and DsA. Tables S8 and S9 list a detailed assignment of experimental and theoretical vibrational frequencies of H_3L and DsA, respectively.

Table 1. Molecular orbitals involved in the main transitions originating the UV-Vis spectrum of DsA.

Wavelength (nm)	Oscillator Strength	Molecular Orbitals		Natural Transition Orbitals [a]	
296.2	(0.1719)	HOMO-1 → LUMO	95.9%	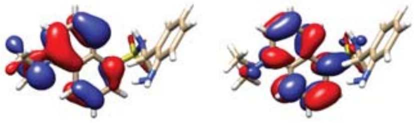	(96%)
220.8	(0.3030)	HOMO-1 → LUMO+1 HOMO-4 → LUMO HOMO-3 → LUMO+1 HOMO-3 → LUMO	38.3% 31.9% 13.1% 7.5%	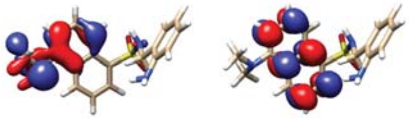 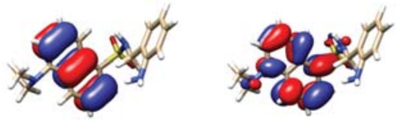	(56%) (39%)
195.8	(0.3430)	HOMO-3 → LUMO+1 HOMO-6 → LUMO HOMO-4 → LUMO	46.3% 25.2% 9.3%	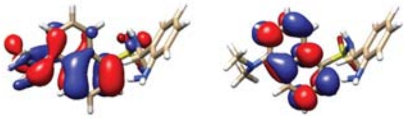 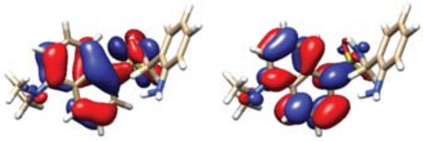	(50%) (37%)
187.1	(0.4146)	HOMO-4 → LUMO+1 HOMO-3 → LUMO+1 HOMO-1 → LUMO+3	73.4% 8.8% 6.2%	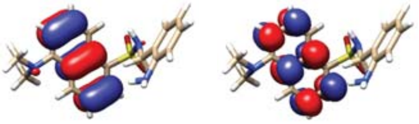	(83%)
174.6	(0.2974)	HOMO-2 →LUMO+2 HOMO → LUMO+4 HOMO → LUMO+5 HOMO-8 → LUMO	55.4% 9.0% 7.7% 7.1%	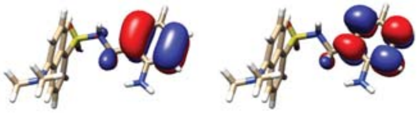 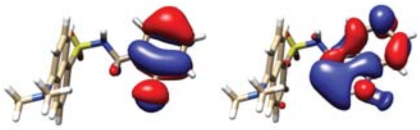	(55%) (18%)

[a] The contributions of the represented NTO pairs to the electronic transitions are given between parenthesis.

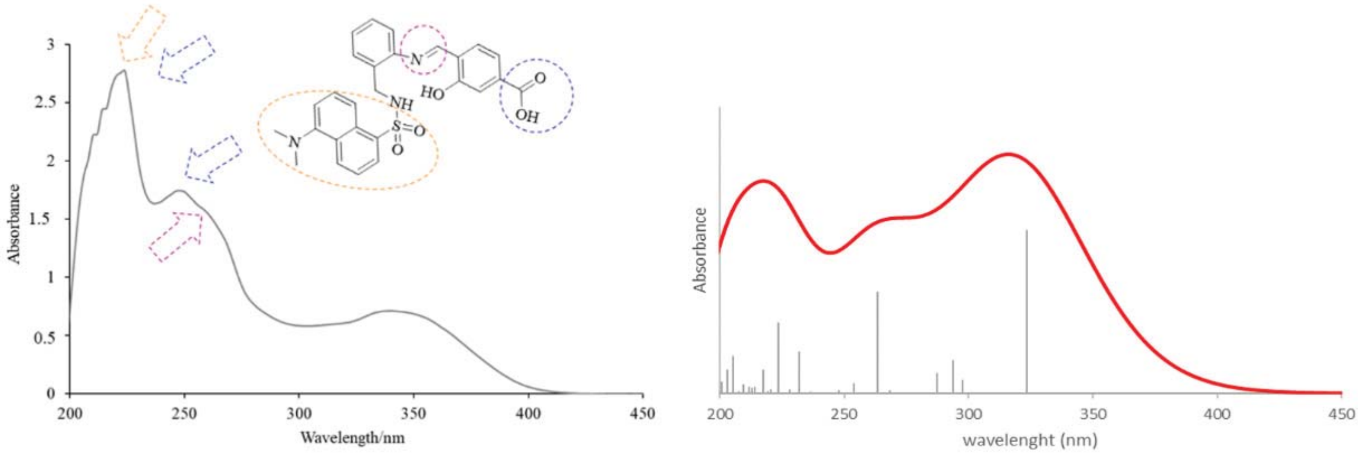

Figure 4. Experimental (**left**) and theoretical (**right**) profiles for the electronic spectrum of H_3L. The signal assignment of the main groups of the molecule has been included as a scheme. The orange arrow shows the bands associated with the dansyl moiety. The blue arrows show the band associated with the carboxylic group and the pink arrow shows the band associated with the azomethine group. Vertical lines indicate individual electronic transitions listed in Table 1.

Table 2. Molecular orbitals involved in the three more intense transitions originating the UV-vis spectrum of H_3L.

Wavelenght (nm)	Oscillator Strength	Molecular Orbitals		Natural Transition Orbitals [a]	
323.4	(0.42700)	HOMO-1 → LUMO HOMO → LUMO	72.3% 19.6%	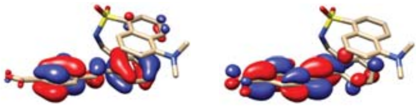	(92%) [a]
263.3	(0.26370)	HOMO-6 → LUMO HOMO-2 → LUMO HOMO-10 → LUMO HOMO-1 → LUMO HOMO-9 → LUMO	26.7% 25.4% 12.3% 6.4% 6.1%	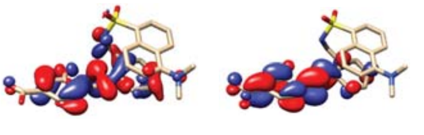	(84%)
223.7	(0.18510)	HOMO-4 → LUMO+1 HOMO → LUMO+2 HOMO-4 → LUMO HOMO-3 → LUMO+1 HOMO → LUMO+4	27.0% 25.1% 6.5% 5.7% 5.4%	 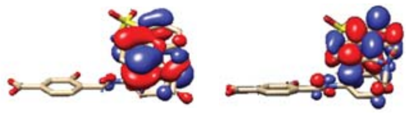	(42%) (33%)

[a] The contributions of the represented NTO pairs to the electronic transitions are given between parenthesis.

Table 3. Experimental and theoretical vibrational frequencies (cm^{-1}) of H_3L.

Experimental [a]	Theoretical [a]	Normal Vibrational Mode Assignment [a]
1145	1109	O=S=O symm stretch
1317	1303	O=S=O asymm stretch + N-H bending + CH_2 bending
1412	1377	C-O-H bending (phenolic ring)
1613	1642	N=C stretch
1686	1796	C=O stretch (COOH group)
3283	3204	O-H stretch (phenol)

[a] The unsigned mean error for these assignments is 43 cm^{-1}.

Table 4. Experimental and theoretical vibrational frequencies (cm^{-1}) of DsA.

Experimental [a]	Theoretical [a]	Normal Vibrational Mode Assignment [a]
1142	1113	O=S=O symm stretch + ring C-H bending (aniline + dansyl)
1310	1310	O=S=O asymm stretch + N-H bending (aniline) + CH_2 twist (aniline)
1630	1601, 1624	NH_2 bending (aniline) + C=C asymm stretch (aniline)
3323	3367	N-H stretch (aniline)
3383	3389	NH_2 symm stretch (aniline)
3470	3484	NH_2 asymm stretch (aniline)

[a] The unsigned mean error for these assignments is 21 cm^{-1}.

2.3. Experimental and Theoretical Studies on the Copper(II) Complex

$Cu_2L_2(H_2O)_4$ was obtained at room temperature from the reaction between H_3L and $Cu(OAc)_2$, and alternatively, by the electrochemical oxidation of a copper anode immersed in a solution of H_3L. It must be noted that the electrochemical procedure saves time and leads to higher yields (see experimental section). The copper(II) complex obtained from H_3L has been investigated in solution by a combination of UV-Vis and fluorescence spectrometries. In the solid state, this complex has been investigated by elemental analysis and ATR-FTIR spectroscopy. Characterization details are shown in the experimental section. The results of the CHNS analyses showed that the copper(II) complex was obtained with a 1:1 metal:ligand stoichiometry. This finding is coherent with the formation of a sulfonamido-bridged dimeric complex, as those reported by us for complexes of related Schiff base ligands [17,33,34].

The IR spectrum of this copper(II) complex showed a broad band centered at about 3360 cm^{-1} attributable to ν(OH), which evidenced the formation of the hydrated complex (Figure S7). The slight shifts of ν(NC), $\nu_{as}(SO_2)$, and $\nu_s(SO_2)$ to lower wavenumbers (1–5 cm^{-1}), as well as the absence of the band related to the phenolic COH bending (1412 cm^{-1}), is a clear sign of the coordination of the Schiff base ligand through its O_{phenol}, N_{imine}, and $N_{sulfonamide}$ donor atoms. The observation of two bands attributable to $\nu_{as}(COO^-)$ and $\nu_s(COO^-)$ at about 1574 and 1393 cm^{-1}, respectively, instead of a single band at 1686 cm^{-1} indicates the deprotonation of the carboxylic group of the ligand in this complex. The net charge zero of the complex can be easily achieved, as the ligand units can adopt the zwitterionic form, in which the carboxylic groups are deprotonated, while the amine N atoms are protonated.

The electronic spectrum of the dimeric copper(II) complex (Figure S8) shows three dominant signals around 219, 244, and 336 nm appearing ca. 5 nm blue-shifted with respect to the free ligand (224, 248, and 340 nm). The metal complexation of H_3L with Cu^{2+} is related to a new absorption band at about 410 nm, and which has been assigned to a ligand-to-metal charge transfer (LMTC).

The observation of a new absorption band at about 680 nm attributable to a *d*-*d* transition ($^2E_g \leftarrow {}^2T_{2g}$) in the UV-Vis spectrum of the dinuclear copper(II) complex (Figure 5), is a sign of six-coordination [35]. Therefore, two water molecules must complete the coordination sphere around each metal ion, occupying the vacant positions left by the dianionic Schiff base ligand.

The geometrical structure of the copper(II) complex has been analyzed by means of theoretical methods. Based on experimental results (CHNS analyses, infrared, and electronic spectra) and previous studies [17,33,34], we were able to obtain the optimized geometry of a sulfonamido-bridged dimeric complex represented in Figure 6. The structure is symmetric, with an inversion center in the middle of the distorted square formed by the two sulfonamido bridges. A detailed analysis of the metal ion environment shows a six-coordination pattern comprising the expected *N*,*N*,*O* binding site of a ligand unit, a sulfonamido *N*-bridge of the neighboring ligand unit, and two monodentate water molecules completing its coordination sphere. A comparison of this optimized structure with a related dimeric copper(II) complex, which is also bridged by sulfonamide N atoms, showed a great similarity. The reported complex shows Cu-N distances in the range 1.969(4)-2.004(4) Å, and bond angles in the range 85.12–98.4 [34].

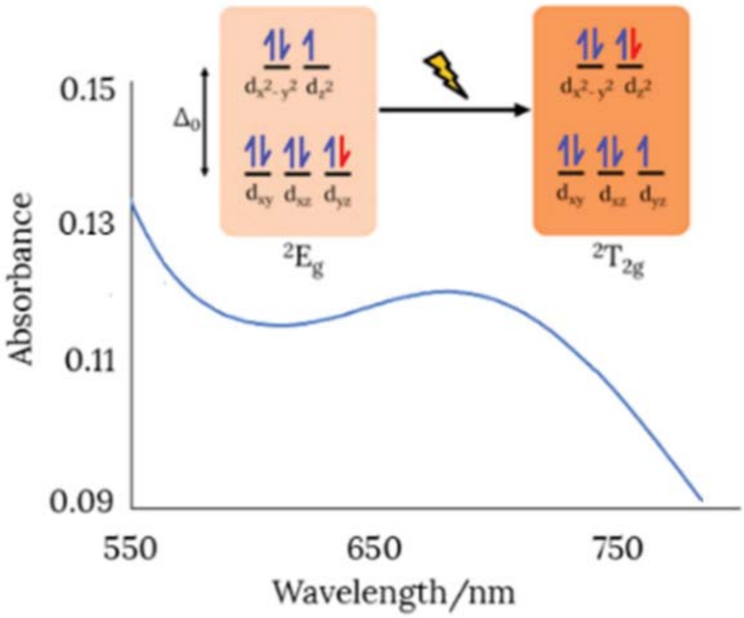

Figure 5. View of the *d-d* transition in the UV-Vis spectrum of the dimeric copper(II) complex (in ethanol).

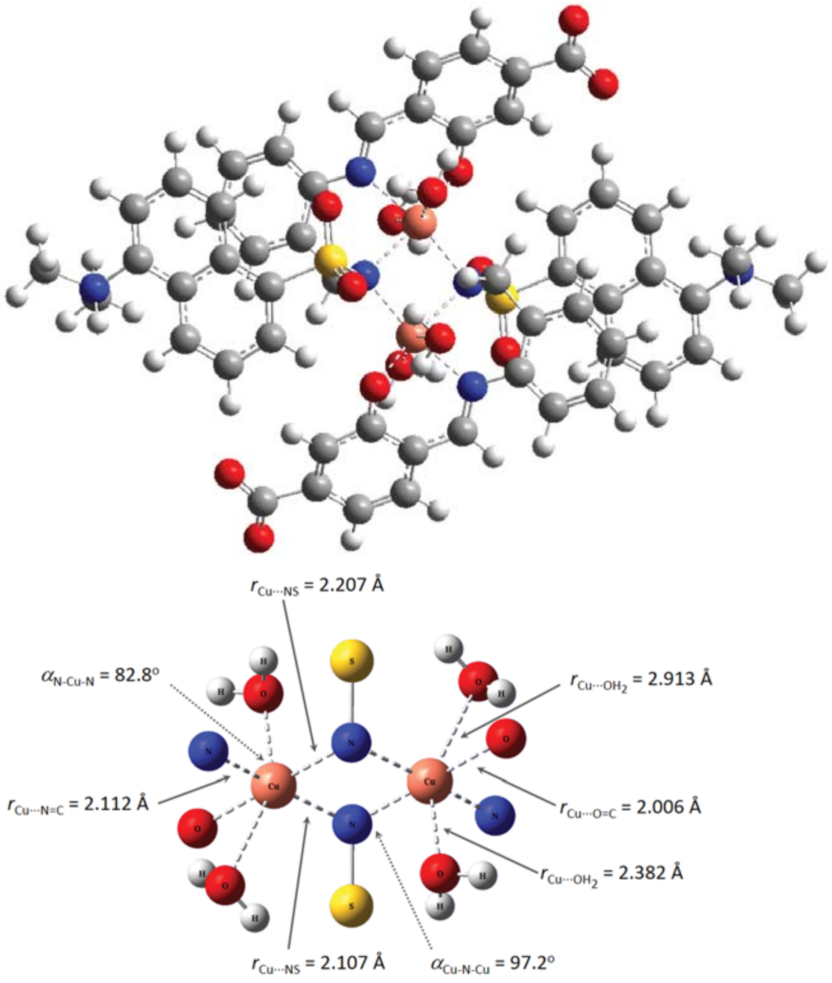

Figure 6. (**Top**): M062X/6-31G* optimized structure of $Cu_2(HL)_2(H_2O)_4$. (**Bottom**): Some bond distances and angles in the coordination environment of the copper ions.

Finally, with the aim of knowing the affinity of H_3L to Cu^{2+} ions at room temperature, the value of the binding constant (K_B) has been determined (Figure S9, K_B = intercept/slope). For this purpose, we used the Benesi–Hildebrand equation [36], using data from the UV-Vis absorption ($K_B = 8.459\ 10^3\ M^{-1}$), as well as from the fluorescence emission intensity ($K_B = 7.190\ 10^3\ M^{-1}$).

Since the reaction of H_3L with Cu^{2+} ions resulted in a decrease of its fluorescence emission, we investigated the quenching mechanism with Stern-Volmer plots [37] ($F_0/F = 1 + K_{SV}[Cu^{2+}]$). Figure S10 shows that the value of the quenching constant decreases with increasing temperature, which is a sign of static quenching. It must be noted that for static quenching ($\tau_0/\tau = 1$), the K_{SV} value matches that of the K_B for the complex formation ($K_{SV} = 9.010\ 10^3\ M^{-1}$). Hence, K_{SV} show similar values to K_B for the reaction of H_3L with Cu^{2+} ions in a 1:1 molar ratio, supporting the accuracy of these measurements.

2.4. Investigations on the Interaction of H_3L with CuO NPs

Spectrofluorimetry, Attenuated Total Reflection-Infrared spectroscopy (ATR-IR), Micro-X-ray Fluorescence (μ-XRF), Scanning Electron Microscopy-Energy Dispersive X-ray spectroscopy (SEM-EDX), and Density Functional Theory (DFT) were used to investigate the reaction product of H_3L with CuO NPs.

2.4.1. Spectrofluorimetry

The interaction of H_3L with CuO NPs leads to the emission of a yellow fluorescence when a solid sample of the reaction product is placed under a light source UV of 365 nm (Figure 7).

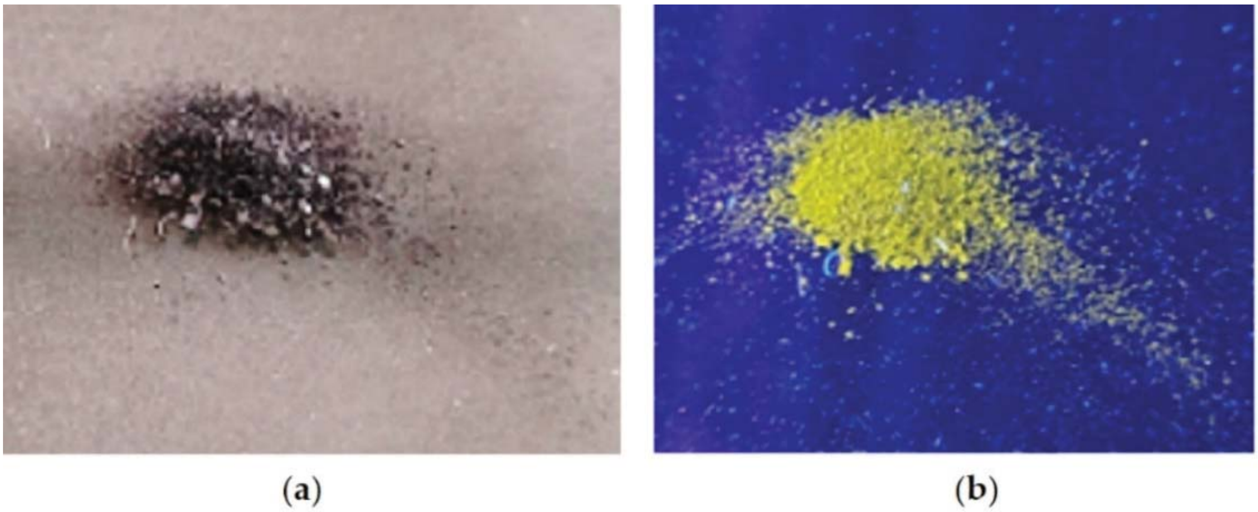

Figure 7. The effect of UV light (365 nm) on a powdery sample of H_3L-CuO NPs; (**a**) under natural light, (**b**) under UV light (365 nm).

The fluorescence spectrum of the product obtained from the reaction between H_3L and CuO NPs revealed a quenching of the fluorescence emission at 524 nm, in comparison with the fluorescence intensity of H_3L measured under similar conditions. Stern-Volmer plots evidenced a static quenching mechanism, and therefore K_{SV} provides a measure of the bonding affinity between H_3L and CuO NPs (Figure 8, top). As expected, K_{SV} for the reactions of H_3L with CuO NPs and Cu^{2+} ions have similar values (Table 5). Values of Gibbs free energy, which have been determined from K_{SV}, indicate that the dimeric copper(II) complex (-22.19 kJ mol^{-1}) and H_3L-CuO NPs (-22.41 kJ mol^{-1}) also show similar stabilities.

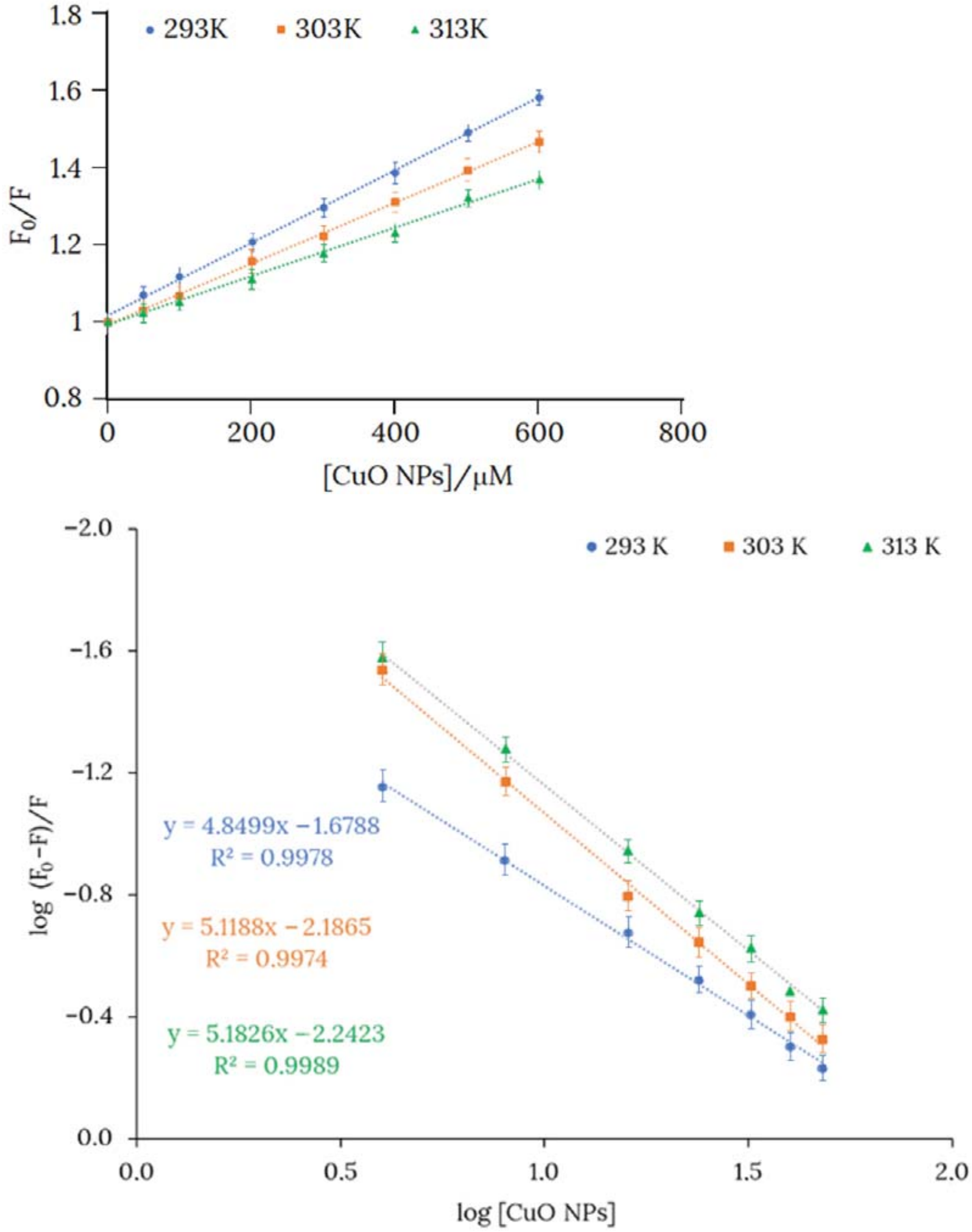

Figure 8. (**Top**): Plots of the intensities of the fluorescence spectra of H_3L (10^{-4} M) vs. [CuO NPs] in an 80:20 ethanol:water solution. Slopes of the curves at 293, 303, and 313 K are Stern-Volmer constants K_{SV} ($K_{SV} = k_q\tau$, where τ is the lifetime of the fluorophore) at the cited temperatures. (**Bottom**): The Scatchard plot for binding H_3L to CuO NPs at 293, 303, and 313 K and pH 11.

Table 5. Values of Gibbs free energy, binding constant, and quenching constant for the reaction of H_3L with Cu^{2+} ions (in 1:1 molar ratio), as well as CuO NPs. Binding constants were obtained from fluorescence emission intensity and UV-Vis absorption.

Species	**ΔG_{Ksv} kJ mol^{-1}**	**$K_{b\ FL}$ M^{-1}**	**$K_{b\ UV\text{-}Vis}$ M^{-1}**	**$K_{sv\ 293\ K}$ M^{-1}**	**$K_{sv\ 303\ K}$ M^{-1}**	**$K_{sv\ 313\ K}$ M^{-1}**
Cu^{2+}	−22.19	7190	8459	9010	7650	6420
CuO NPs	−22.41	-	-	9840	8470	6920

The number of interaction binding sites (n) were determined by the Scatchard Equation (1), where F_0 and F are the relative fluorescence of H_3L in absence and presence of NMs, respectively, K_B is the binding constant, and $[Q]$ is the quencher concentration [38]. The Scatchard equation linear graph of H_3L and NMs is shown in Figure 8 (bottom). The number of binding sites (n) is around 5 at 293 K, suggesting five binding sites for H_3L on the CuO NPs surface. The interaction ratio increased slightly with rising temperature, probably because temperature favors the reactivity of superficial Cu^{2+} ions.

$$\log\left(\frac{F_0 - F}{F}\right) = \log K_B + n\log[Q] \tag{1}$$

2.4.2. Attenuated Total Reflection-Infrared Spectroscopy

The IR spectrum of H_3L-CuO NPs clearly shows the absence of the band at about 3283 cm^{-1} attributable to ν OH/ν NH modes, which evidences the bideprotonation of the Schiff base ligand. Furthermore, a slight shift to lower wavenumbers of the bands corresponding to ν(NC), $\nu_{as}(SO_2)$, and $\nu_s(SO_2)$ can be observed The similarity between the ATR-IR spectra of CuO-H_3L NPs and $Cu_2(HL)_2(H_2O)_4\cdot 10H_2O$ (Figure 9) indicates that the interaction between H_3L and NMs surface occurs via metal-ligand coordination through the $N_{sulfonamide}$, N_{imine}, and O_{phenol} atoms. The observation of two bands attributable to $\nu_{as}(COO^-)$ and $\nu_s(COO^-)$ at about 1574 and 1391 cm^{-1}, respectively, is a clear sign of the deprotonation of the carboxyl group present in the ligand, which is coherent with the formation of the carboxylate sodium salt.

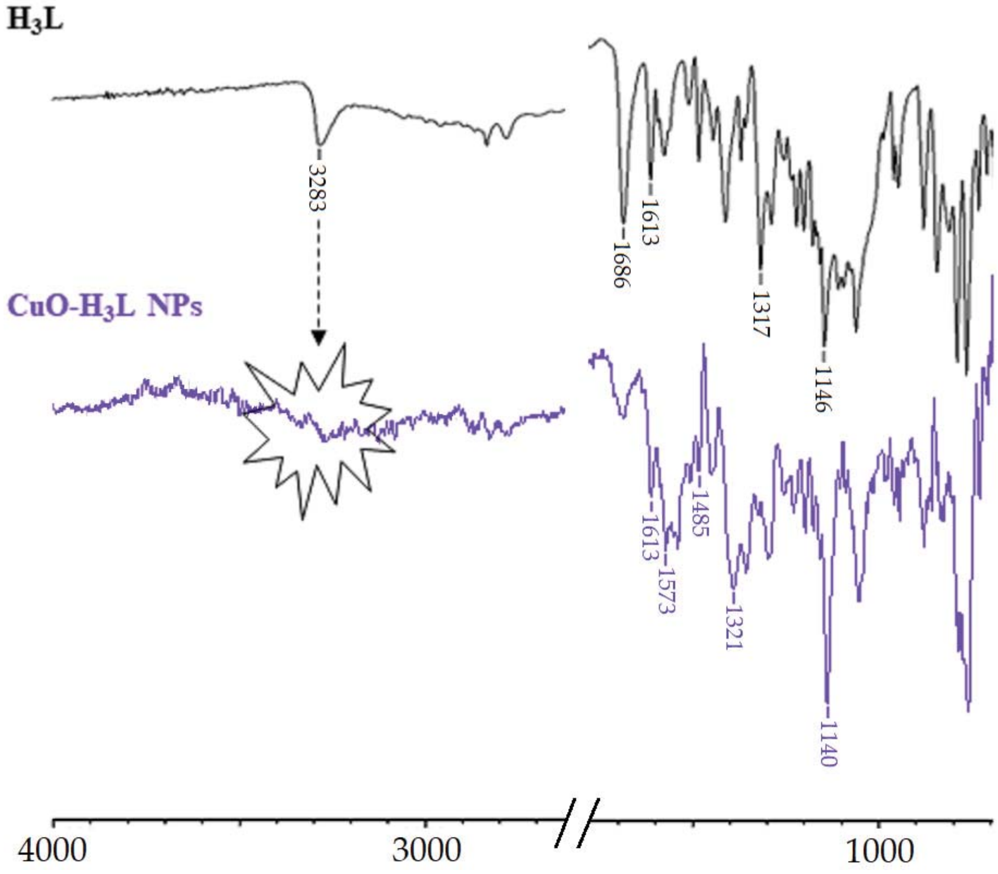

Figure 9. Partial view of the ATR-FTIR spectra of the free ligand (top) and CuO-H_3L NPs.

2.4.3. Micro-X-ray Fluorescence

Figure 10 shows the peaks corresponding to the characteristic X-ray fluorescence emission of the chemical elements present in the reaction product of CuO NPs with H_3L.

The µ-XRF analysis indicates that the polycrystalline sample of CuO-H_3L NPs contains copper and sulfur in a 30:1 ratio by weight, which is coherent with a 15:1 molar ratio (CuO:H_3L). Moreover, µ-XRF mapping was used to explore the distribution of copper and sulfur within a sample of CuO-H_3L NPs (Figure 10, inset). The homogeneity observed supports the effective interaction between the CuO NPs and H_3L.

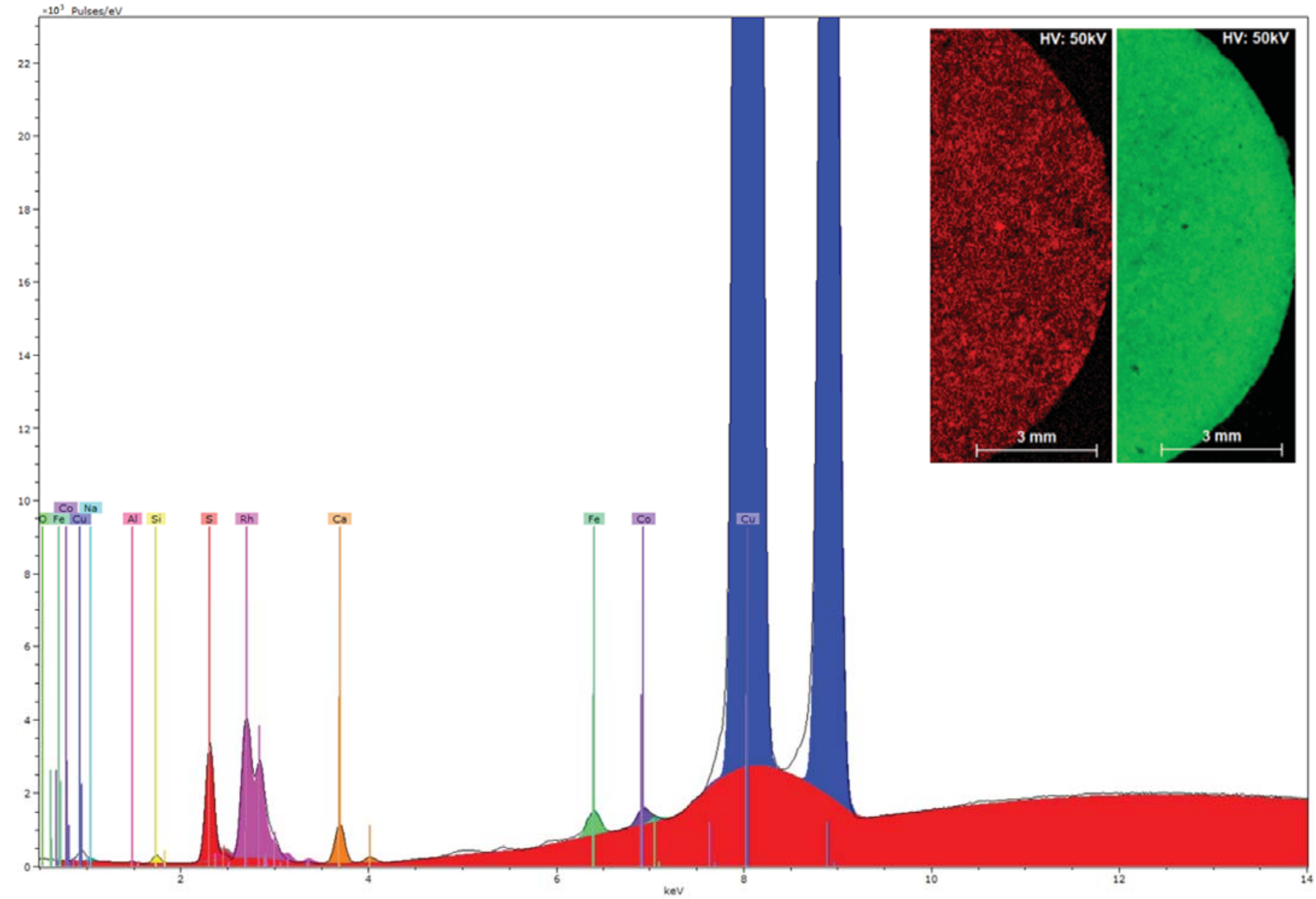

Figure 10. XRF spectrum of the reaction product of CuO NPs with H_3L. *X* axis: energy (keV), *Y* axis: intensity. Inset: XRF mapping of the reaction product between CuO NPs and H_3L with elemental distribution of sulfur (red) and copper (green) on the sample surface.

2.4.4. Scanning Electron Microscopy-Energy Dispersive X-ray Spectroscopy

The SEM micrograph shown in Figure 11 show that the NPs are agglomerated to form clusters, which are made up of nanocrystals of sizes in the range of 70 to 40 nm, with a rather irregular shape.

A combination of SEM and EDX has been used to generate a "map" of element distributions in the raw sample. The EDX analysis shows the uniform presence of Cu, O, C, N, S, and Na elements with similar spatial distribution patterns, which supports the interaction of H_3L (as carboxylate sodium salt) with CuO NPs.

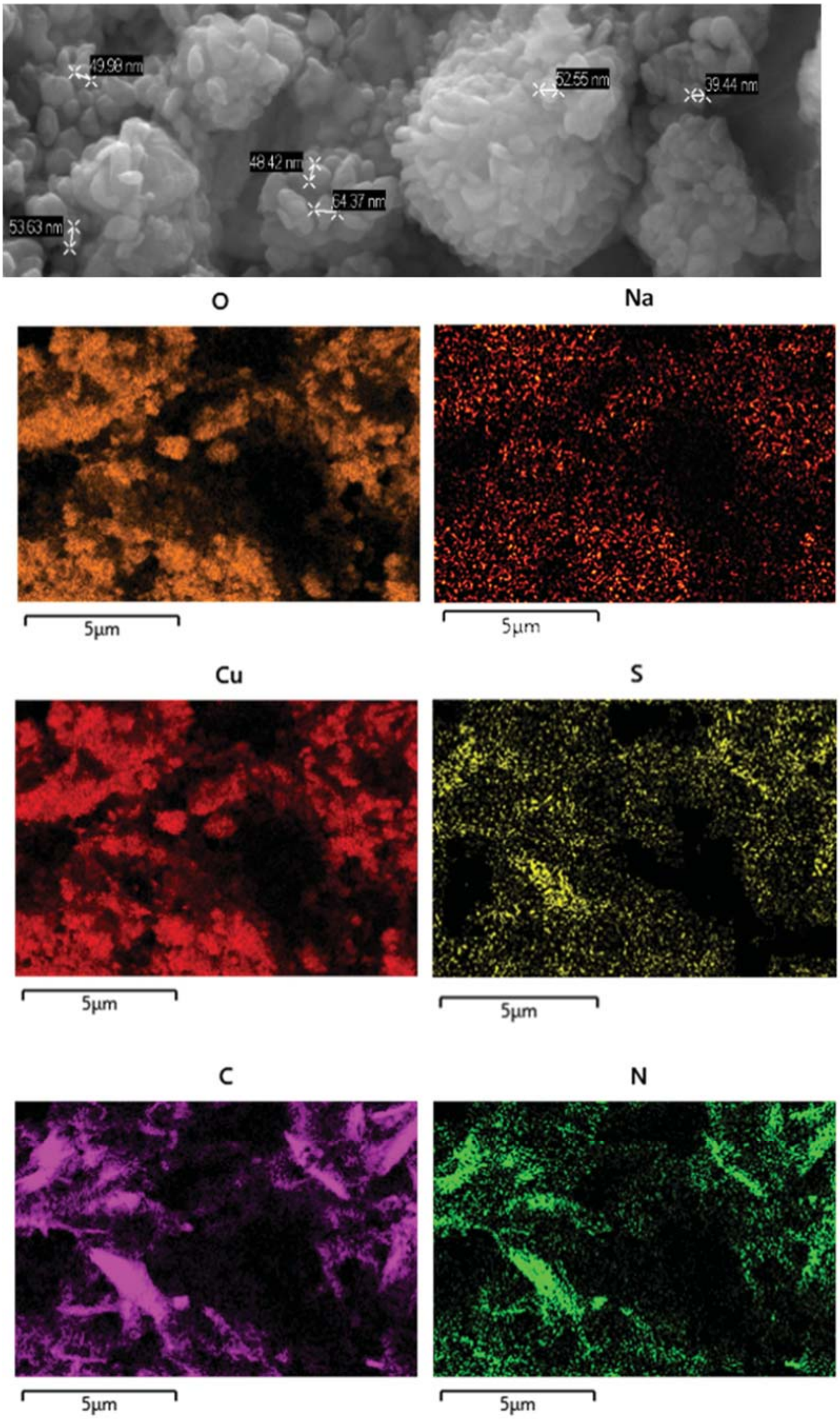

Figure 11. (**Top**): SEM micrograph of H_3L-CuO NPs. (**Bottom**): EDX mapping pattern of the element distribution: Cu, O, S, N, C, and Na.

2.4.5. DFT Studies

Several models have been considered to mimic the interaction between H_3L and CuO NPs using DFT calculations [39] (Figure S11). The largest models studied comprise a single unit of the ligand interacting with a sheet of 32 units of CuO. The geometry of these surfaces has been taken from one of its common crystallographic structures (available from CSD) and choosing that facet containing the largest number of copper atoms suitable to interact with the ligand, in this case, the (1,0,0) facet. The size of the largest models has been chosen to allow a complete interaction between H_3L and the NPs surface. Particular attention has been devoted to establishing the preference of a dianionic (as phenolate and sulfonamide anion) or a monoanionic (only as phenolate) form of the ligand to interact with the superficial Cu^{2+} ions on the NPs. Figure 12 shows the DFT models for the interaction of CuO NPs with these dianionic and monoanionic forms of the ligand.

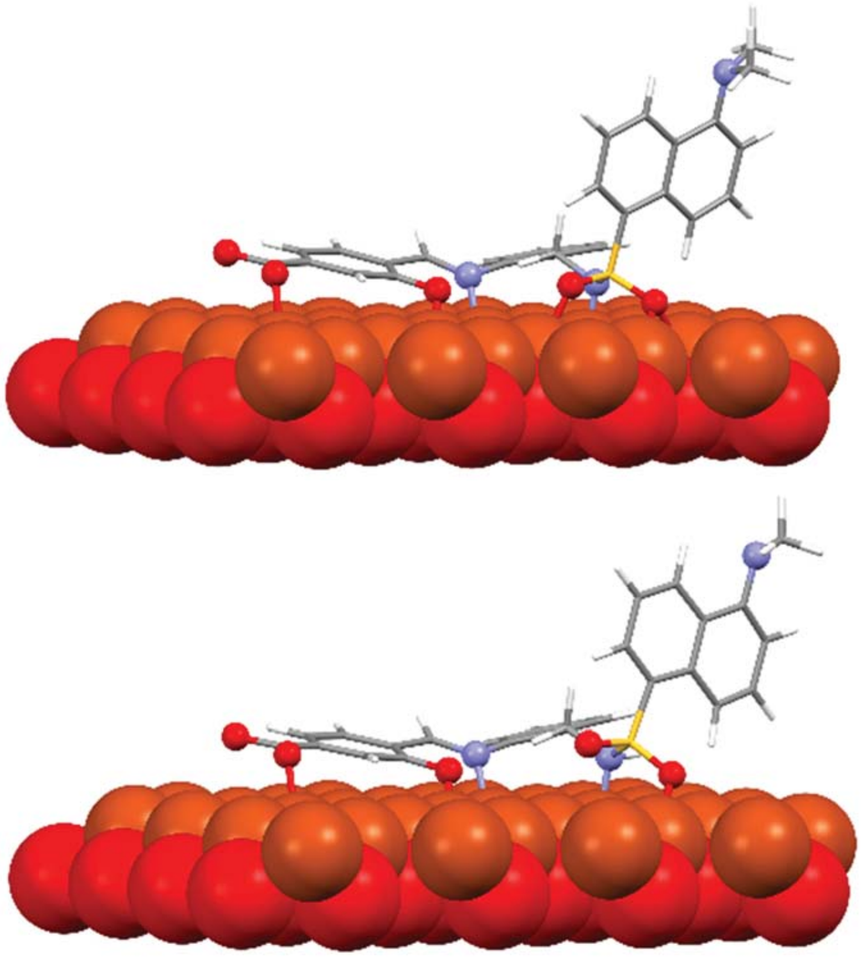

Figure 12. DFT models for the interaction H_3L-NPs.

As a result of these CuO NP models, we can deduce that the interactions of the dianionic form of the ligand show higher stabilization energies (−273.4 kcal/mol) than those corresponding to the monoanionic ones (−170.0 kcal/mol). A similar trend is observed for all the diverse models considered, even with the smallest models employed here, which only consider the interaction between the ligand and a single CuO unit (Figure S11). These theoretical results confirm that the interaction between H_3L and the NMs surface takes place through the O_{phenol}, N_{imine}, and $N_{sulfonamide}$ atoms of the ligand, as occurring for the dimeric copper(II) complex. In addition, the interactions of the superficial Cu^{2+} ions with the oxygen atoms of the carboxylate and the sulfonamide groups appear to contribute to the stabilization of the systems studied.

2.5. Fluorescence Emission Studies on H_3L upon Addition of CuO NPs

In order to check the usefulness of H_3L as a chemosensor for the detection of CuO NPs, we selected a concentration of H_3L of 126 ppb. The fluorescence emission varied linearly in the range 0–10.5 ppm with the gradual addition of CuO NPs. Concentration values of CuO NPs higher than those indicated would oversaturate the system. The decrease by over 90% in the fluorescence emission of ethanol-water solutions (in 80:20 *v*/*v*) of H_3L (λ_{em} = 540 nm) upon addition of CuO NPs (λ_{em} = 538 nm) is shown in Figure 13.

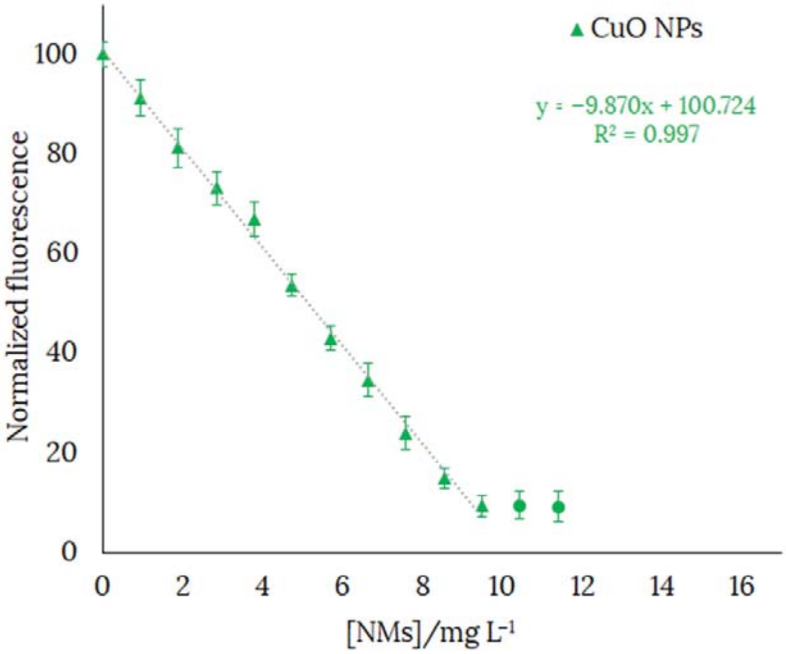

Figure 13. Fluorescence emission spectra calibration curve of H_3L in 80:20 ethanol:water solution at pH 11, with gradual addition of CuO NPs (until the fluorescence intensity stops decreasing). $[H_3L]$ = 126 ppb. NaOH 0.1 M was used to deprotonate H_3L. Final volume of the solution = 4 mL. Each solution was sonicated for 1 min before being measured. λ_{exc} = 400 nm.

The limit of detection (LOD) and the limit of quantification (LOQ) of H_3L have been expressed as LOD = 3SD/M and LOQ = 10SD/M, where SD is the standard deviation of the response and M is the slope of the calibration curve. LOD and LOQ were 330 ppb and 1.09 ppm, respectively. It must be noted that these values are higher than those previously reported by us for a pyrrole-based Schiff base ligand (13.83 μgL^{-1} and 46.05 μgL^{-1}, respectively) [17] and a phenol-based Schiff ligand (9.8 μgL^{-1} and 32.6 μgL^{-1}, respectively) [18]. The working range of H_3L has been obtained using LOQ, as the minimum value that can be measured, and the highest value of [NMs] at which linearity is still maintained, as the maximum value. Therefore, the working range for detection of CuO NPs with $[H_3L]$ = 126 ppb was 1.1–9.5 ppm.

In view of the affinity of H_3L to CuO NPs, we studied the selectivity of H_3L as a probe for the cited NPs. As a criterion for interference, a ±10% variation of the average fluorescence intensity was used. The selectivity of H_3L as a probe for CuO NPs was tested in the presence of common metal ions in water, such as Na^+, K^+, Mg^{2+}, Ca^{2+}, Fe^{3+}, and Al^{3+} metal ions, in the same concentration as CuO NPs (Figure 14). These results showed that the cited species do not significantly interfere with the detection of CuO NPs. Al^{3+} ions can be tolerated in concentrations of at least 4 ppm without interference.

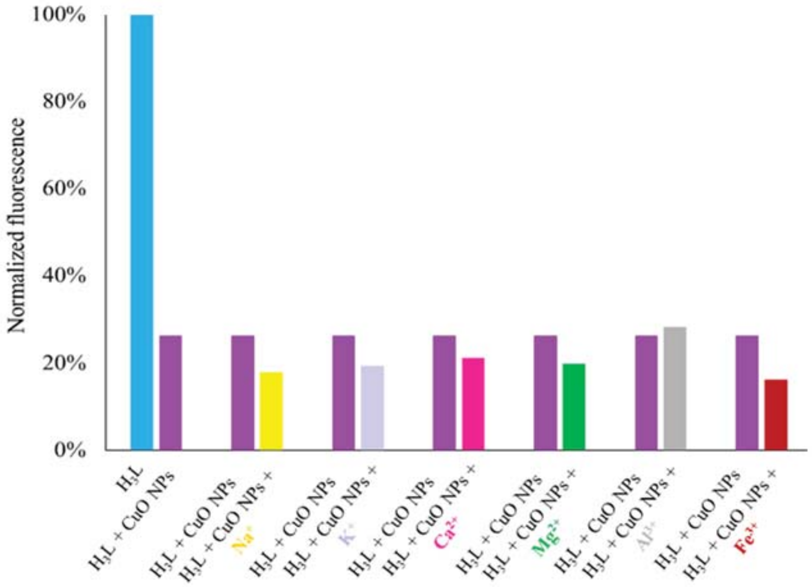

Figure 14. Fluorescence responses of H_3L (2.5 nM, 1.26 ppb) toward CuO NPs (8 ppm) in the presence of some common metal ions (top) such as Na^+ (8 ppm), K^+ (8 ppm), Mg^{2+} (8 ppm), Ca^{2+} (8 ppm), Fe^{3+} (8 ppm), and Al^{3+} (4 ppm). All experiments were performed in 4 mL of an ethanol–water solution in 80:20 *v/v* (pH 11) under λ_{exc} = 400 nm.

3. Materials and Methods

All starting materials and reagents were commercially available, and they were used without further purification. ^{1}H NMR spectra (400 MHz) were measured in deuterated solvents using a Varian Inova 400 Spectrometer. *J* values are given in Hertz. The IR spectra were measured in the range 4000 to 400 cm^{-1} wavenumber using a FTIR spectrometer PerkinElmer Spectrum Two coupled with Platinum Diamond ATR, which consists of a diamond disc as an internal reflection element. Elemental analyses were performed on an elemental analyzer FISONS model EA 1108. Fluorescence emission studies were performed on a Shimadzu RF-600 Spectro Fluorophotometer. X-ray fluorescence was measured under vacuum (19.6 mbar) using an M4 TORNADO system (BRUKER), with the Rh tube, operating at 50 kV and 200 μA. The fluorescence maps were collected for a total time of 2 ms per pixel, with a pixel size of 20 μm. Scanning Electron Microscopy (SEM) was applied to investigate the size and morphology of the NPs, and it was carried out under a ZEISS FESEM ULTRA Plus with EDX microanalysis.

3.1. Sample Preparation

Samples for investigations on the interaction of H_3L with CuO NPs were obtained by stirring an ethanol solution of H_3L at pH 9, and a suspension of NPs in a 2:1 molar ratio, at room temperature for about 15 min. Then, the sample was air-dried for about 48 h.

3.2. Crystal Structure Analysis Data

Diffraction data for prismatic crystals corresponding to DsA and H_3L were collected at 100(2) K, using graphite-monochromatized Mo-*Kα* radiation (λ = 0.71073 Å) from a fine focus sealed tube, using a Bruker D8 Venture Photon III-14 diffractometer. Data were routinely processed and corrected for Lorentz and polarization effects. Multi-scan absorption corrections were performed using the SADABS routine [40]. The structure was solved by standard direct methods using SHELXT [41], and then refined by full matrix least squares on F^2 by using the SHELXL program [42]. All non-hydrogen atoms were anisotropically refined. Hydrogen atoms were mostly included in the structure factor calculation in geometrically idealized positions, with thermal parameters depending on the parent atom, by using a riding model. H atoms potentially involved in H-bonding were localized in Fourier maps and then refined with a thermal parameter depending on the parent N atom. More details of the refinement, as well as crystal data are collected in Table S1 of the ESI.

CCDC 2,121,699 and 2,121,700 contain the supplementary crystallographic data for this paper. These data can be obtained free of charge from the Cambridge Crystallographic Data Centre via www.ccdc.cam.ac.uk/data_request/cif (accessed on 20 September 2022)

3.3. Computational Methods

Theoretical calculations on DsA, H_3L, copper(II) complex, and ligand-NPs models have been performed employing density functional theory (DFT) methods, as implemented in Gaussian 09 [39]. Thus, M062X/6-31G* geometrical optimization of different starting structures of DsA, H_3L, and its copper(II) complex have been performed. The most stable conformers found have been characterized by calculation of their vibrational frequencies. For DsA and H_3L, we tested the idea that the M062X/6-31G* level provided results of comparable quality to those obtained with a more extended basis set as 6-311++G** (not included for brevity), but with a significantly smaller computational cost. For comparison with the experiment results, the theoretical IR spectra of DsA and H_3L have been obtained using the harmonic vibrational frequencies scaled by 0.947 and a FWHM of 4 cm^{-1}.

The electronic spectra of DsA and H_3L have been obtained employing the M062X/6-31G* level, and the influence of the solvent has been included using the PCM method and $\varepsilon = 24.852$ for ethanol. The main electronic transitions have been analyzed by computing their natural transition orbitals, which provide a picture of the orbitals involved in any electronic transition, which is easier to interpret [43].

Models of different size have been used to evaluate the interaction of the ligand with CuO NPs. The geometry for the smallest model, comprising only one H_3L unit and a single CuO unit, has been optimized without restrictions. In the remaining cases, the geometries of the ligand over the surface have been freely optimized, keeping a frozen structure for the metal obtained from crystallographic data.

Interaction energies, E_{int}, for these systems have been evaluated as $E_{int} = E_{complex} - (E_{H3L} + E_{metal\ model})$, where the $E_{complex}$ is the total energy of the interacting ligand-NPs, E_{H3L} is the total energy of the monoanionic or dianionic form of the H_3L ligand, and E_{metal} is the energy of the different metal models indicated above. These interaction energies have been evaluated by means of the NEDA method included in the NBO7.0 program [44], so that the basis set superposition error is corrected by means of the counterpoise method.

3.4. Synthesis and Characterization of Compounds

3.4.1. DsA

The compound *N*-(2-aminobenzyl)-5-(dimethylamino)naphthalene-1-sulfonamide was prepared following a synthetic procedure previously used with imidazolopyridine compounds [45], but with some modifications. In a 250 mL round flask, 2.35 mmol (0.6339 g) of dansyl chloride was dissolved in 60 mL of CH_2Cl_2. In a second flask, 2.59 mmol (0.3162 g) of the 2-aminobenzylamine was dissolved in 40mL of CH_2Cl_2, at which 2.59 mmol (0.2631 g) of triethylamine was added. The content of the second flask was added to the dansyl chloride solution, giving a dark yellow solution which was stirred at room temperature for 18 h. During this time period, the solution changed its color from dark to light yellow. Evaporation under reduced pression of the solution to a third of its volume, and the addition of diethyl ether until the observation of turbidity, led to the formation of a light brown precipitate, which is a small unreacted 2-aminobenzylamine fraction. Filtration of the mixture led to the separation of 2-aminobenzylamine as a powdery solid. Evaporation to dryness under vacuum of the filtrate led to the precipitation of a light yellow powdery solid, which was washed with deionized water to separate triethylamine hydrochloride. The yellow solid was filtrated and air-dried to be characterized as DsA.

Yield: 0.793 g (95%). ^1H NMR (400 MHz, dmso-d_6, δ in ppm): δ 8.47 (d, 1H), 8.35 (d, 1H), 8.24 (t, 1H), 8.14 (d, 1H), 7.62 (t, 1H), 7.60 (t, 1H), 7.27 (d, 1H), 6.94 (d, 1H), 6.92

(t, 1H), 6.58 (d, 1H), 6.43 (t, 1H), 4.87 (s, 2H), 3.85 (d, 2H), 2.84 (s, 6H). UV-Vis (ethanol, 4.02 10^{-5} mol L^{-1}, λ in nm, ε in parenthesis) 252 (67,262 $M^{-1}cm^{-1}$), 294 (14,754 $M^{-1}cm^{-1}$), 346 (19,322 $M^{-1}cm^{-1}$). Fluorescence λ/nm: λ_{em} 520 (λ_{ex} 336, ethanol, bandwidth of 5 nm). ATR-FTIR (ν in cm^{-1}): 3472 w (ν_{as} HNH), 3384 m (ν_s HNH), 3323 m (ν NH), 1632 m (δ HNH), 1309 s (ν_{as} OSO), 1143 s (ν_s OSO). Elemental analysis (found): C 63.8; H 5.9; N 11.8; S 8.5%; Calc. for $C_{19}H_{21}N_3O_2S$: C, 64.2; H, 6.0; N, 11.8; S, 9.0% (Mw: 355.5 g·mol^{-1}).

3.4.2. H_3L

H_3L was prepared following a synthetic procedure previously used by us [19]. In a 250 mL round-bottomed flask, 0.104 g of DsA (0.29 mmol) was dissolved in 60 mL of absolute ethanol. Then, while the solution was being stirred, 4-formyl-3-hydroxybenzoic acid (0.034 g, 0.29 mmol) in absolute ethanol (30 mL) was added. A light-yellow solution was obtained, which was stirred at room temperature for 24 h. Then, the solution was concentrated in a rotary evaporator to dryness, and a yellow precipitate was obtained. Then, hexane was added to wash the precipitate. This was filtered under vacuum and an orangey-colored precipitate is obtained, which was left to dry under vacuum for a couple of hours. The crude solid was purified by column chromatography. We used hexane:ethyl acetate (50:50) to extract the unreacted DsA, and methanol to extract H_3L.

Yield: 0.120 g (82%); ^{1}H NMR (400 MHz, dmso-d_6) δ 13.18 (s, 1H), 12.29 (s, 1H), 8.66 (s, 1H), 8.38 (t, 1H), 8.36 (d, 1H), 8.26 (d, 2H), 8.02 (d, 1H), 7.72 (d, 1H), 7.49 (d, 1H), 7.48 (t, 1H), 7.47 (t, 1H), 7.44 (s, 1H), 7.27 (d, 1H), 7.23 (t, 1H), 7.19 (d,1H), 7.09 (d, 1H), 7.08 (t, 1H), 4.19 (d, 2H), 2.81 (s, 6H). UV-Vis (absolute ethanol, 10^{-3} mol L^{-1}, λ in nm, ε in parenthesis) 224 (2,770 $M^{-1}cm^{-1}$), 248 (1,743 $M^{-1}cm^{-1}$), 260 (1,550 $M^{-1}cm^{-1}$), 340 (711 $M^{-1}cm^{-1}$). Fluorescence λ/nm: λ_{em} = 510 (λ_{ex} = 400, ethanol, bandwidth of 5 nm). ATR-IR (ν in cm^{-1}): 3283 m (ν NH), 1686 s (ν CO), 1613 m (ν CN), 1412 m (δ COH), 1317 s (ν_{as} OSO), 1146 s (ν_s OSO). Elemental analysis (found): C 57.0; H 4.8; N 7.3; S 5.3%; Calc. for $C_{27}H_{25}N_3O_5S{\cdot}HCl{\cdot}H_2O$: C, 58.0; H, 5.4; N, 7.5; S, 5.7% (Mw: 558.1 g·mol^{-1}).

3.4.3. $Cu_2(HL)_2(H_2O)_4{\cdot}10H_2O$

Method 1: The copper(II) complex was obtained at room temperature by electrochemical oxidation of a metal anode immersed in an acetonitrile solution (75 mL) of H_3L (0.05 g, 0.01 mmol), containing tetraethylammonium perchlorate (ca. 20 mg) as a supporting electrolyte (Caution: Although no problem has been encountered in this work, all perchlorate compounds are potentially explosive and should be handled in small quantities and with great care!). This was electrolyzed for about 1h and 3 min at a current intensity of 5.0 mA and an initial voltage of 9.4 V. The suspension so obtained was concentrated in a rotary evaporator to dryness, and a dark-green precipitate was obtained. Then, the powdery solid was washed with deionized water, filtered, and air-dried (yield = 54%).

Method 2: An ethanol solution (60 mL) of H_3L (0.04 g, 0.08 mmol) was added to 50 mL of an ethanol solution of $Cu(OAc)_2{\cdot}H_2O$ (0.0158 g, 0.0794 mmol). The resulting solution was stirred in a round-bottomed flask of 250 mL for 3 h at room temperature. The color of the solution changed from pale yellow to dark brown during the reaction time. The suspension obtained was evaporated to dryness under vacuum. Then, the powdery solid was washed with diethyl ether, filtered, and air-dried (yield = 37%).

ATR-IR (ν in cm^{-1}): 3393 br (ν OH, ν NH), 1612 m (ν CN), 1574 s (ν_{as} OCO), 1392 s (ν_s OCO), 1314 s (ν_{as} OSO), 1119 s (ν_s OSO). UV-Vis (ethanol, λ in nm) 219, 244, 336, 414. Fluorescence λ/nm: λ_{em}= 530 (λ_{ex}= 400, ethanol, bandwidth of 15 nm). Elemental analysis (found): C 46.9; H 5.3; N 6.3; S 4.6%; calc. for $C_{54}H_{54}Cu_2N_6O_{14}S_2{\cdot}10H_2O$: C, 46.9; H, 5.4; N, 6.1; S, 4.6 (Mw: 1382.4 g mol^{-1}).

4. Conclusions

The crystal structures of H_3L and DsA were elucidated, and a detailed assignment of the most significant bands of both UV-Vis and infrared spectra has been done on the basis of the calculated spectra using density functional theory (DFT) methods. The DFT-optimized geometry of $Cu_2L_2(H_2O)_4$ shows a six-coordination environment comprising a *N,N,O* binding site of a ligand unit, a sulfonamido N-bridge of the neighboring ligand unit, and two water molecules completing its coordination sphere. The affinity of H_3L to react with Cu^{2+} ions in solution, giving rise to $Cu_2L_2(H_2O)_4$ (K_B = 9.01 10^3 L mol^{-1}), is similar to that found for the interaction with Cu^{2+} ions on the surface of CuO NPs (K_B = 9.84 10^3 L mol^{-1}). Values of Gibbs free energy indicate that the dimeric copper(II) complex (−22.19 kJ mol^{-1}) and H_3L-CuO NPs (−22.41 kJ mol^{-1}) also have similar stabilities. Fluorescence spectroscopic measurements suggest five binding sites for H_3L on the CuO NPs surface. The μ-XRF analysis indicates that the polycrystalline sample of CuO-H_3L NPs contains copper and sulfur in a 30:1 ratio by weight, which is coherent with a 15:1 molar ratio (CuO:H_3L). The EDX mapping of the element distribution shows the uniform presence of Cu, Na O, C, N, and S elements with a similar spatial distribution pattern, supporting the existence of the interaction of H_3L (as carboxylate sodium salt) with CuO NPs. ATR spectroscopy shows the bideprotonation of the Schiff base ligand, as well as a slight shift to lower wavenumbers of the bands corresponding to ν(NC), $\nu_{as}(SO_2)$, and $\nu_s(SO_2)$, which demonstrates the chelating behavior of the Schiff base ligand. DFT studies confirm that the interaction between H_3L and the NMs surface takes place through the O_{phenol}, N_{imine}, and $N_{sulfonamide}$ atoms of the dianionic ligand (as phenolate and sulfonamide anion), as occurring for the copper(II) complex.

We probed that at room temperature and basic pH, the fluorescence intensity of H_3L in aqueous solution decreased linearly with increasing concentration of CuO NPs. A solution of H_3L (126 ppb) shows sensitive responses to CuO NPs, with a limit of detection (LOD) as low as 330 ppb, and a working range between 1.1 and 9.5 ppm. H_3L possesses selectivity toward CuO NPs in the presence of common metal ions in water, such as Na^+, K^+, Mg^{2+}, Ca^{2+}, Fe^{3+}, and Al^{3+} ions.

Supplementary Materials: The following supporting information can be downloaded at: https://www.mdpi.com/article/10.3390/ijms231911565/s1.

Author Contributions: Conceptualization, J.S.-M. and P.B.-B.; methodology, Y.A.-I.; software, I.P.-J., A.M.G.-D. and Y.A.-I.; validation, J.S.-M., I.P.-J. and P.B.-B.; formal analysis, I.P.-J., M.F., A.M.G.-D. and Y.A.-I.; investigation, I.P.-J., A.M.G.-D. and Y.A.-I.; resources, J.S.-M. and P.B.-B.; data curation, I.P.-J.; writing—original draft preparation, J.S.-M. and Y.A.-I.; writing—review and editing, A.M.G.-D.; visualization, M.F.; supervision, J.S.-M.; project administration, P.B.-B.; funding acquisition, P.B.-B. All authors have read and agreed to the published version of the manuscript.

Funding: This research was funded by the Ministerio de Ciencia, Innovación y Universidades (RTI2018-099222-B-I00) and Interreg Atlantic Area, Poctep (ACUINANO Project).

Institutional Review Board Statement: Not applicable.

Informed Consent Statement: Not applicable.

Data Availability Statement: Not applicable.

Acknowledgments: Authors would like to thank the use of RIAIDT-USC analytical facilities, and the support provided for this work.

Conflicts of Interest: The authors declare no conflict of interest.

References

1. Siddiqi, K.S.; Husen, A. Current status of plant metabolite-based fabrication of copper/copper oxide nanoparticles and their applications: A review. *Biomater. Res.* **2020**, *24*, 11. [CrossRef] [PubMed]
2. Grigore, M.E.; Biscu, E.R.; Holban, A.M.; Gestal, M.C.; Grumezescu, A.M. Methods of Synthesis, Properties and Biomedical Applications of CuO Nanoparticles. *Pharmaceuticals* **2016**, *9*, 75. [CrossRef] [PubMed]
3. Gawande, M.B.; Goswami, A.; Felpin, F.X.; Asefa, T.; Huang, X.; Silva, R.; Zou, X.; Zboril, R.; Varma, R.S. Cu-Based Nanoparticles: Synthesis and Applications in Catalysis. *Chem. Rev.* **2016**, *116*, 3722–3811. [CrossRef]
4. Ighalo, J.O.; Sagboye, P.A.; Umenweke, G.; Ajala, O.J.; Omoarukhe, F.O.; Adeyanju, C.A.; Ogunniyi, S.; Adeniyi, A.G. CuO nanoparticles (CuO NPs) for water treatment: A review of recent advances. *Environ. Nanotechnol. Monit. Manag.* **2021**, *15*, 100443. [CrossRef]

5. Cuong, H.N.; Pansambal, S.; Ghotekar, S.; Oza, R.; Hai, N.T.T.; Viet, N.M.; Nguyen, V.-H. New frontiers in the plant extract mediated biosynthesis of copper oxide (CuO) nanoparticles and their potential applications: A review. *Environ. Res.* **2022**, *203*, 111858. [CrossRef]
6. Karlsson, H.L.; Toprak, M.S.; Fadeel, B. Toxicity of metal and metal oxide nanoparticles. In *Handbook on the Toxicology of Metals*, 5th ed; Nordberg, G.F., Costa, M., Eds.; Academic Press: Cambridge, MA, USA, 2022; pp. 87–126. ISBN 9780128232927. [CrossRef]
7. Rajput, V.; Minkina, T.; Ahmed, B.; Sushkova, S.; Singh, R.; Soldatov, M.; Laratte, B.; Fedorenko, A.; Mandzhieva, S.; Blicharska, E.; et al. Interaction of Copper-Based Nanoparticles to Soil, Terrestrial, and Aquatic Systems: Critical Review of the State of the Science and Future Perspectives. *Rev. Environ. Contam. Toxicol.* **2020**, *252*, 51–96. [CrossRef]
8. Rotini, A.; Gallo, A.; Parlapiano, I.; Berducci, M.T.; Boni, R.; Tosti, E.; Prato, E.; Maggi, V.; Cicero, A.M.; Migliore, L.; et al. Insights into the CuO nanoparticle ecotoxicity with suitable marine model species. *Ecotoxicol. Environ. Saf.* **2018**, *147*, 852–860. [CrossRef]
9. Croteau, M.-N.; Misra, S.K.; Luoma, S.N.; Valsami-Jones, E. Bioaccumulation and toxicity of CuO nanoparticles by a freshwater invertebrate after waterborne and dietborne exposures. *Environ. Sci. Technol.* **2014**, *48*, 10929–10937. [CrossRef]
10. Wu, F.; Harper, B.J.; Crandon, L.E.; Harper, S.L. Assessment of Cu and CuO nanoparticle ecological responses using laboratory small-scale microcosms. *Environ. Sci. Nano* **2020**, *7*, 105–115. [CrossRef]
11. Assadian, E.; Zarei, M.H.; Gilani, A.G.; Farshin, M.; Degampanah, H.; Pourahmad, J. Toxicity of Copper Oxide (CuO) Nanoparticles on Human Blood Lymphocytes. *Biol. Trace Elem. Res.* **2018**, *184*, 350–357. [CrossRef]
12. Naz, S.; Gul, A.; Zia, M. Toxicity of copper oxide nanoparticles: A review study. *IET Nanobiotechnol.* **2020**, *14*, 1–13. [CrossRef] [PubMed]
13. Navarro-Pacheco, N.I.; Roubalova, R.; Dvorak, J.; Benada, O.; Pinkas, D.; Kofronova, O.; Semerad, J.; Pivokonsky, M.; Cajthaml, T.; Bileja, M.; et al. Understanding the toxicity mechanism of CuO nanoparticles: The intracellular view of exposed earthworm cells. *Environ. Sci. Nano* **2021**, *8*, 2464–2477. [CrossRef]
14. Zhao, J.; Ren, W.; Dai, Y.; Liu, L.; Wang, Z.; Yu, X.; Zhang, J.; Wang, X.; Xing, B. Uptake, distribution, and transformation of CuO NPs in a floating plant *Eichhornia crassipes* and related stomatal responses. *Environ. Sci. Technol.* **2017**, *51*, 7686–7695. [CrossRef] [PubMed]
15. Peng, C.; Xu, C.; Liu, Q.; Sun, L.; Luo, Y.; Shi, J. Fate and transformation of CuO nanoparticles in the soil–rice system during the life cycle of rice plants. *Environ. Sci. Technol.* **2017**, *51*, 4907–4917. [CrossRef]
16. Navratilova, J.; Praetorius, A.; Gondikas, A.; Fabienke, W.; Kammer, F.V.D.; Hofmann, T. Detection of Engineered Copper Nanoparticles in Soil Using Single Particle ICP-MS. *Int. J. Environ. Res. Public Health* **2015**, *12*, 15756–15768. [CrossRef]
17. Sanmartín-Matalobos, J.; García-Deibe, A.M.; Fondo, M.; Zarepour-Jevinani, M.; Domínguez-González, M.R.; Bermejo-Barrera, P. Exploration of an easily synthesized fluorescent probe for detecting copper in aqueous samples. *Dalton Trans.* **2017**, *46*, 15827–15835. [CrossRef]
18. Sanmartín-Matalobos, J.; García-Deibe, A.M.; Zarepour-Jevinani, M.; Aboal-Somoza, M.; Bermejo-Barrera, P.; Fondo, M. Exploring the Chelating Potential of an Easily Synthesized Schiff Base for Copper Sensing. *Crystals* **2020**, *10*, 235. [CrossRef]
19. Sanmartín-Matalobos, J.; Bermejo-Barrera, P.; Alves-Iglesias, Y.; García-Deibe, A.M.; Fondo, M. Synthesis and Characterization of a Dansyl-Based Fluorescent Probe for Analytical Purposes. *Chem. Proc.* **2022**, *8*, 76. [CrossRef]
20. Ahumada, M.; Lazurko, C.; Alarcon, E.I. Fundamental concepts on surface chemistry of nanomaterials. In *Photoactive Inorganic Nanoparticles. Micro and Nano Technologies*; Pérez Prieto, J., González Béjar, M., Eds.; Elsevier: Amsterdam, The Netherlands, 2019; pp. 1–19. [CrossRef]
21. Owen, J.S. The coordination chemistry of nanocrystal surfaces. *Science* **2015**, *347*, 615–616. [CrossRef]
22. De Roo, J.; De Keukeleere, K.; Hens, Z.; Van Driessche, I. From ligands to binding motifs and beyond; the enhanced versatility of nanocrystal surfaces. *Dalton Trans.* **2016**, *45*, 13277–13283. [CrossRef]
23. Liu, P.; Qin, R.; Fu, G.; Zheng, N. Surface Coordination Chemistry of Metal Nanomaterials. *J. Am. Chem Soc.* **2017**, *139*, 2122–2131. [CrossRef] [PubMed]
24. Srivastava, P.; Ali, R.; Razi, S.S.; Shahid, M.; Patnaik, S.; Misra, A. A simple blue fluorescent probe to detect Hg^{2+} in semiaqueous environment by intramolecular charge transfer mechanism. *Tetrah. Lett.* **2013**, *54*, 3688–3693. [CrossRef]
25. Bhatt, P.; Govender, T.; Krugera, H.G.; Maguire, G.E.M. *N*-Benzyl-5-(di-methyl-amino)-naphthalene-1-sulfonamide. *Acta Cryst.* **2011**, *E67*, o2458–o2459. [CrossRef]
26. Qiu, L.; Jiang, P.; He, W.; Tu, C.; Lin, J.; Li, Y.; Gao, X.; Guo, Z. Structural and fluorescent study of zinc complexes of dansyl aminoquinoline. *Inorg. Chim. Acta* **2007**, *360*, 431–438. [CrossRef]
27. Zhou, S.; Zhou, Z.-Q.; Zhao, X.-X.; Xiao, Y.-H.; Xi, G.; Liu, J.-T.; Zhao, B.-X. A dansyl based fluorescence chemosensor for Hg2+ and its application in the complicated environment samples. *Spectrochim. Acta A Mol. Biomol. Spectrosc.* **2015**, *148*, 348–354. [CrossRef]
28. Patrascu, B.; Mocanu, S.; Coman, A.; Madalan, A.M.; Popescu, C.; Paun, A.; Matache, M.; Ionita, P. Synthesis of Fluorescent Dansyl Derivatives of Methoxyamine and Diphenylhydrazine as Free Radical Precursors. *Int. J. Mol. Sci.* **2020**, *21*, 3559. [CrossRef]
29. Celedón, S.; Roisnel, T.; Artigas, V.; Fuentealba, M.; Carrillo, D.; Ledoux-Rak, I.; Hamon, J.-R.; Manzur, C. Palladium(II) complexes of tetradentate donor–acceptor Schiff base ligands: Synthesis and spectral, structural, thermal and NLO properties. *New J. Chem.* **2020**, *44*, 9190–9201. [CrossRef]
30. Fondo, M.; Doejo, J.; García-Deibe, A.M.; Sanmartín-Matalobos, J.; Vicente, R. A Ni_8 metallacalix[4]arene and a Cu_4 molecular rhomboid: Limiting the nuclearity of carboxysalen-like metal complexes. *CrystEngComm* **2016**, *35*, 6673–6682. [CrossRef]

31. Fondo, M.; Doejo, J.; García-Deibe, A.M.; Ocampo, N.; Sanmartín, J. Carboxylic decorated Schiff base complexes as metallotectons for hydrogen bonded 3D networks. *Polyhedron* **2015**, *101*, 78–85. [CrossRef]
32. Sanmartín, J.; Novio, F.; García-Deibe, A.M.; Fondo, M.; Bermejo, M.R. Trimorphism of an asymmetric disulfonamide Schiff base. *New J. Chem.* **2007**, *31*, 1605–1612. [CrossRef]
33. Sanmartín-Matalobos, J.; Portela-García, C.; Fondo, M.; García-Deibe, A.M.; Llamas-Saiz, A.L. A simple route to dinuclear complexes containing unusual μ-$N_{sulfonamido}$ bridges. *J. Coord. Chem.* **2016**, *69*, 1358–1370. [CrossRef]
34. Sanmartín, J.; Novio, F.; García-Deibe, A.M.; Fondo, M.; Ocampo, N.; Bermejo, M.R. Dimeric Complexes of a Tridentate Schiff Base Ligand–Crystal Structure of a Cu^{II} Complex with Uncommon μ_2-$N_{sulfonamido}$ Bridges and Ferromagnetic Behaviour. *Eur. J. Inorg. Chem.* **2008**, *2008*, 1719–1726. [CrossRef]
35. Blasco, S.; Burguete, M.I.; Clares, M.P.; García-España, E.; Escorihuela, J.; Luis, S.V. Coordination of Cu^{2+} ions to C_2 symmetric pseudopeptides derived from valine. *Inorg. Chem.* **2010**, *49*, 7841–7852. [CrossRef] [PubMed]
36. Alves, J.Q.; Máximo, L.N.C.; Franco, L.P.; Silva, R.S.D.; Oliveira, M.F.D. Fluorescence-quenching CdTe quantum dots applied for identification of cocaine-structure analogues. *Anal. Methods* **2019**, *11*, 185–191. [CrossRef]
37. Lakowicz, J.R. *Principles of Fluorescence Spectroscopy*, 3rd ed.; Springer: Baltimore, MD, USA, 2006.
38. Moeno, S.; Nyokong, T. Opposing responses elicited by positively charged phthalocyanines in the presence of CdTe quantum dots. *J. Photochem. Photobiol. A* **2009**, *201*, 228–236. [CrossRef]
39. Frisch, M.J.; Trucks, G.W.; Schlegel, H.B.; Scuseria, G.E.; Robb, M.A.; Cheeseman, J.R.; Scalmani, G.; Barone, V.; Petersson, G.A.; Nakatsuji, H.; et al. *Gaussian 09, Revision, A.02*; Gaussian Inc.: Wallingford, CT, USA, 2016.
40. Sheldrick, G.M. *SADABS, Area-Detector Absorption Correction*; Siemens Industrial Automation, Inc.: Madison, WI, USA, 2001.
41. Sheldrick, G.M. SHELXT—Integrated space-group and crystal-structure determination. *Acta Crystallogr. Sect. A Found. Adv.* **2015**, *71*, 3–8. [CrossRef]
42. Sheldrick, G.M. Crystal structure refinement with SHELXL. *Acta Crystallogr. Sect. C Struct. Chem.* **2015**, *71*, 3–8. [CrossRef]
43. Martin, R.L. Natural transition orbitals. *J. Chem. Phys.* **2003**, *118*, 4775–4777. [CrossRef]
44. Glendening, E.D.; Badenhoop, J.K.; Reed, A.E.; Carpenter, J.E.; Bohmann, J.A.; Morales, C.M.; Karafiloglou, P.; Landis, C.R.; Weinhold, F. *NBO 7.0*; Theoretical Chemistry Institute, University of Wisconsin: Madison, WI, USA, 2018.
45. Edwards, P.J.; Martina, S.L.X.; Andrews, M.J.I.; Bar, G.L.J.; Allart, B.; Burritt, A.; Tao, X.; Kroll, F.E.K. Imidazolopyridine Compounds Useful for the Treatment of Degenerative and Inflammatory Diseases. PCT/EP2007/063108, 5 June 2008.